

Emission of twisted light from quantum dot arrays with a discrete rotational symmetry

H. T. Sullivan* and J. H. Cole†

*ARC Centre of Excellence in Exciton Science and Chemical and Quantum Physics,
School of Science, RMIT University, Melbourne, Australia*

(Dated: August 11, 2020)

We theoretically explore the optical properties of a circular array of quantum dots. This structure, that we call a circular emitter array (CEA), can exchange optical angular momentum via the emission and absorption of circularly polarised light as well as light carrying orbital angular momentum. Analytical expressions are derived for both interband and intraband transition rates and selection rules are determined. Only the key properties of the quantum dots are considered when modelling the CEA. This extends the applicability of our model to CEAs composed of a variety of quantum dots. Finally design principles for the tuning of the specific optical properties of the CEA are determined. This opens up the prospect of the designing a metamaterial, consisting of a surface of CEAs, that upconverts optical angular momentum.

I. INTRODUCTION

Radiation has two sources of angular momentum. The commonly understood source is the polarisation of the light. Circularly polarised photons are endowed with an angular momentum of $\sigma\hbar$, where $\sigma = \pm 1$ ^{1,2}. This angular momentum is commonly referred to as spin angular momentum (SAM). Light can also derive an angular momentum from an azimuthal phase dependence³. This angular momentum is known as orbital angular momentum (OAM). It provides light with a helical phase front and, consequentially, is referred to as *twisted light*. The OAM of a photon is $\ell\hbar$ where ℓ is an unbounded integer. Twisted light beams that have Laguerre-Gaussian and Bessel function radial profiles have been extensively studied^{4,5}; both have the same azimuthal phase dependence which is encoded mathematically as $e^{i\ell\phi}$. Twisted light beams may also be circularly polarised providing each photon a total angular momentum of $(\ell \pm \sigma)\hbar$.

Twisted light has found a great range of applications⁶, including applying high optical torques to microparticles⁷, 3D surface imaging⁸, atomic trapping⁹ and novel motion detection methods for microscopic particles¹⁰. The larger alphabet of states that may be encoded into twisted photons promises a marked increase in the capacity of optical communication¹¹. Similarly, this enhanced information content of twisted photons have made them attractive as possible qubits to the quantum information community¹².

The maturation of the field has been accompanied by a growing interest in new methods to generate twisted light. Transmitting regular light through a hologram is the most common method to generate orbital angular momentum in light¹³. However, now a considerable number of metamaterials have been constructed that can generate twisted light on the microscopic scale¹⁴⁻¹⁶. This new field of research includes the design and fabrication of various microscopic structures that can emit twisted light^{17,18}; some of which enable tuning the OAM of the optical emissions¹⁹.

One particular quantum structure that has been theoretically explored is the system of discrete emitters arranged in a circular array. The emitters are in close enough proximity to form a delocalised state across the whole system. Quasi-momenta arises in this system as momentum is a conserved by discrete, rather than continuous, translations. This system we refer to as a circular emitter array (CEA). It can emit and absorb twisted light²⁰⁻²². Some arrays that meet the physical requirements to be CEAs have already been fabricated. These include semiconductor quantum dots arranged in close proximity through a growth and etching technique²³, gold nanospheres connect by DNA ligands²⁴ and a variety of other systems²⁵.

Some research suggests that CEAs could mediate the upconversion of optical angular momentum^{26,27}. That is, the angular momentum of consecutive light pulses could be absorbed by the CEA and then released in a single optical emission. Figure 1 demonstrates this process. A metamaterial composed of CEAs could form the basis for a device which would allow upconversion to occur without relying on a mediating crystal with a nonlinear light-matter interaction. The same metamaterial has been suggested to provide the foundation for an OAM laser²⁰. Whilst quantum dot lasers are well understood and eminently useful²⁸, research into the lasing capacities of novel quantum structures is still limited.

A number of authors have suggested that molecular arrays could provide the physical system for the CEA^{20-22,26}. A molecular CEA presents great difficulties in engineering the specific states, energy levels and the light-matter interaction. Another proposal utilised cylindrical waveguides arranged in a circle²⁹. Whilst the authors provide further theory demonstrating the feasibility of a CEA, this particular system could not be implemented on a metamaterial due to its three-dimensional nature. This limits its potential applications. Others have theoretically investigated CEAs composed of three semiconductor quantum dots (QD) and have shown them capable of absorbing and re-emitting circularly polarised

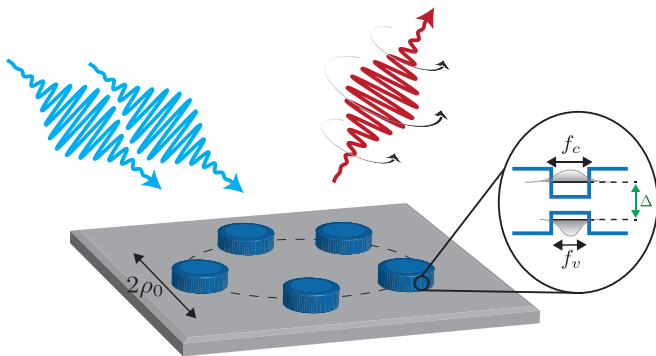


FIG. 1. A five site CEA absorbs two circularly polarised photons and upconverts the combined angular momentum through the emission of a twisted photon. The radius the QDs are located at from the centre of the CEA is ρ_0 . Each quantum dot individually has a valence and conduction band wave function; associated with these wave functions are full width half maximums f_v and f_c , respectively. Electrons in the valence band experience greater confinement and therefore have a narrower full width half maximum. The first photon the CEA absorbs is approximately the same energy as the QD band gap, Δ , whilst the second photon's energy is that required for transitions within the conduction band. Both photons are circularly polarised with combined angular momentum $+2\hbar$. The emitted twisted photon carries away this angular momentum which is distributed as SAM = $-\hbar$ and OAM = $+3\hbar$.

light of the opposite handedness³⁰. This system is the theoretically simplest and experimentally the most realisable; however, the authors do not investigate its capacity to emit or absorb twisted light.

This paper considers CEAs composed of semiconductor QDs. Our research utilises the extensive literature on twisted light semiconductor systems. Research in this area has already developed a general theory of semiconductors and twisted light^{31,32}; as well as theory specifically applied to QDs of different geometries^{33,34}, quantum rings³⁵ and quantum wells³⁶. This body of research provides the framework that we use to explore the complete optical properties of CEAs.

The existing literature on CEAs makes a number of assumptions to ascertain the system's optical properties. The primary assumption made is that, within the CEA, electric dipoles are formed between each neighbouring emitter; then, the light emitted from the CEA is calculated as the summation of the light emitted from each individual dipole²⁰⁻²². Our calculation does not make this assumption. Rather, we start from the CEA's total wave function and utilise a semi-classical formalism to compute the probability of certain transitions involving particular optical emissions. Studying a CEA composed of QDs allows us to incorporate the already developed theory of semiconductor quantum structures interacting with twisted light.

Finally, this paper aims to provide the design principles for engineering a CEA, or similar system, with certain op-

tical properties. The only empirical parameters required to utilise our research is the full width half maximum of the wave function of the QD as well as the CEA's energy spectra. With this knowledge, we can compute the necessary geometry of the CEA required for particular optical properties.

II. CIRCULAR EMITTER ARRAY MODEL

The wave function

The delocalised electronic wave function of the CEA is the product of a slowly varying envelope function and a unit cell function $u(\mathbf{r})$. These two functions give two length scales to the system: the envelope functions varies steadily across the entire CEA whilst the the unit cell function is periodic between cells and therefore rapidly oscillates across the CEA. The envelope function is separable into a transverse function in the xy plane $\phi(\mathbf{r}_\perp)$ and a function that varies vertically, $Z(z)$ (the QDs are arranged in xy plane around the z axis). We assume the QDs to be sufficiently confined in the z axis that only a single Z state exists in each band. We restrict our model to a two band model - one valence and one conduction band - which is consistent with similar semiconductor twisted light systems³⁵. The CEA wave function is

$$\psi_{q\nu}(\mathbf{r}) = [\phi_{q\nu}(\mathbf{r}_\perp)Z_\nu(z)] u_\nu(\mathbf{r}). \quad (1)$$

The quantum number q specifies the quasi-angular momentum of the transverse envelope function whilst ν indicates the band. The particle's spin has been ignored.

The transverse envelope function depends on the specific geometry of the CEA. We model a CEA consisting of N QDs exhibiting the C_N symmetry. The distance from the origin to the centre of any QD is ρ_0 . It is assumed that only the interaction between the nearest QDs is significant. The Hamiltonian we employ accounts for both the on-site and coupling energy of the QDs in each band

$$H_0 = \sum_\nu \left[\hbar\omega_\nu \sum_j c_{j\nu}^\dagger c_{j\nu} + t_\nu \sum_{\langle i,j \rangle} \left(c_{i\nu}^\dagger c_{j\nu} + \text{h.c.} \right) \right], \quad (2)$$

where $\hat{c}_{j\nu}^{(\dagger)}$ represents the fermionic annihilation (creation) operator of the j^{th} QD in the band ν . The overlap between the QDs wave functions determines the hopping strength t_ν . The energy difference between the ground states of the valence and conduction bands is $\Delta = \hbar\omega_c - \hbar\omega_v$.

We work in the basis set where there exists a single state localised around each QD in each band. The basis state of QD j in the band ν is denoted $|\chi_{j\nu}\rangle$. The eigenstates of the CEA then take the form

$$|q\nu\rangle = \frac{1}{\sqrt{N}} \sum_j \varepsilon^{(j-1)q} |\chi_{j\nu}\rangle, \quad (3)$$

where $\varepsilon = \exp(i2\pi/N)$. The eigenstates in each band are superpositions comprised of each basis state multiplied by a phase ε^q different from its neighbouring QDs. The range of quasi-angular momentum available to the states of a CEA with an odd number of QDs is $q = [-(N-1)/2, (N-1)/2]$. The triple quantum dot (which is the $N = 3$ CEA) has been found to have these same eigenstates³⁷.

The eigenstates have the corresponding energy

$$E_{q\nu} = \hbar\omega_\nu + 2t_\nu \cos\left(\frac{2\pi q}{N}\right). \quad (4)$$

It is necessary to know the wave function of the CEA to compute its optical properties. Thus, we assume a Gaussian function as the spatial wave function for each QD. Many different QDs have a great variety of wave functions which are not Gaussian³⁸; however, the Gaussian function does adhere to the most general characteristics of the ground states of most QDs. That is, radial symmetry and monotonic decrease from the centre of the QD. We define the spatial wave function of the QD j in band ν as

$$\langle \mathbf{r}_\perp | \chi_{j\nu} \rangle = \chi_{j\nu}(\mathbf{r}_\perp) = \frac{1}{\sqrt{\pi}\varsigma_\nu} e^{-\frac{(\mathbf{r}_\perp - \mathbf{r}_j)^2}{2\varsigma_\nu^2}}. \quad (5)$$

The location of the j^{th} QD is $\mathbf{r}_j = \rho_0 \hat{\boldsymbol{\rho}} + \theta_j \hat{\boldsymbol{\theta}}$ where $\theta_j = 2\pi/N(j-1)$. The confinement of the function is determined by ς_ν . This in turn determines the full width half maximum for the basis function in band ν

$$f_\nu = \varsigma_\nu \sqrt{2 \log 2}. \quad (6)$$

The transverse envelope function of the CEA then takes the form

$$\phi_{q\nu}(\mathbf{r}_\perp) = \mathcal{A}_{q\nu} \sum_j \chi_{j\nu}(\mathbf{r}_\perp) \varepsilon^{(j-1)q}. \quad (7)$$

where the normalisation $\mathcal{A}_{q\nu}$ is calculated in Appendix A.

The Interaction Hamiltonian

We are interested in calculating transitions between two states within the CEA mediated by optical emission or absorption. Fermi's Golden rule states that the rate of a certain transition is proportion to the Hamiltonian matrix element between the initial and final state. We therefore constrain our analysis to determining the magnitude of these matrix elements. We use the minimal coupling interaction Hamiltonian

$$H = \frac{1}{2m} [\mathbf{p} - e\mathbf{A}(\mathbf{r})]^2 - eU(\mathbf{r}) + V(\mathbf{r}), \quad (8)$$

where the electron's effective mass, charge and momentum are denoted m , e and \mathbf{p} , respectively. The potential

that confines the electron $V(\mathbf{r})$ is determined by the geometry of the CEA. The optical response appears as an external scalar and vector potential, $U(\mathbf{r})$ and $\mathbf{A}(\mathbf{r})$.

From here we drop the A^2 term as being too small to contribute. We recognise the system Hamiltonian as $H_0 = \frac{p^2}{2m} + V(\mathbf{r})$. We work in the Lorenz gauge which allows us to set $U(\mathbf{r}) = 0$. This leaves an interaction Hamiltonian of the form

$$H_I = -\frac{e}{2m} (\mathbf{p} \cdot \mathbf{A} + \mathbf{A} \cdot \mathbf{p}). \quad (9)$$

Typically the Coulomb gauge is chosen to eliminate first term in Eq. (9). We work in the Lorenz gauge so that Laguerre-Gaussian modes appear as solutions to the paraxial Maxwell's equation. These modes are characterised by two numbers. The first number, ℓ , defines the OAM of the mode. The second number determines the number of concentric rings of the mode. We set this number to zero to ensure only a single ring profile. This reflects the geometry of the CEA which consists a single ring of QDs, thus making it improbable that its optical emissions could consist of multiple rings. This radial profile of the light's vector potential takes a particularly simple form in the $z = 0$ plane

$$A_\ell(\mathbf{r}_\perp, z = 0) = \sqrt{\frac{2}{\pi\ell!}} \frac{1}{w_0} \left(\frac{\sqrt{2}r}{w_0}\right)^{|\ell|} e^{-r^2/w_0^2} e^{i\ell\theta}, \quad (10)$$

where the beam waist in the $z = 0$ plane is w_0 . The strong vertical confinement of the QDs allows us to assume the optical fields are, effectively, spatially homogeneous across the CEA vertically. This allows for the dipole approximation to be utilised which results in only needing to consider the optical fields in the same vertical plane as the CEA. Hence, from here on, we consider the vector potential only in this plane and use the shorthand notation $A_\ell(\mathbf{r}_\perp, z = 0) \equiv A_\ell(\mathbf{r}_\perp)$.

The vector potential of the optical response then takes the form

$$\mathbf{A}_{\sigma\ell}(\mathbf{r}_\perp, t) = \hat{\varepsilon}_\sigma A_\ell(\mathbf{r}_\perp) e^{-i\omega t} + \text{c.c} = \mathbf{A}_{\sigma\ell}^{(+)}(\mathbf{r}_\perp, t) + \mathbf{A}_{-\sigma-\ell}^{(-)}(\mathbf{r}_\perp, t), \quad (11)$$

where we define the polarisation as $\hat{\varepsilon}_\sigma = \frac{1}{\sqrt{2}}(\hat{\mathbf{x}} + i\sigma\hat{\mathbf{y}})$. The optical response is circularly polarised light when $\sigma = \pm 1$. The part of the vector potential $\mathbf{A}_{\sigma\ell}^{(+)}(\mathbf{r}, t)$ accounts for transitions mediated by an optical emission with SAM = σ and OAM ℓ ; whereas its complex conjugate permits a transition driven by the absorption of light with SAM = $-\sigma$ and OAM $-\ell$.

III. OPTICAL MATRIX ELEMENTS

We now turn our focus to explicitly computing matrix elements for transitions from an initial state with quasi-angular momentum p in band μ to the final state with quasi-angular momentum q in band ν . To simplify this

calculation we break down the matrix element into two parts.

$$\begin{aligned} M &= \langle q\nu | H_I | p\mu \rangle \\ &= -\frac{e}{2m} \langle q\nu | (\mathbf{p} \cdot \mathbf{A} + \mathbf{A} \cdot \mathbf{p}) | p\mu \rangle \\ &= M_1 + M_2. \end{aligned} \quad (12)$$

Although M_1 and M_2 appear to have similar forms, they are distinguished by the object that the momentum operator acts on. In M_1 it acts on Laguerre Gaussian radial mode. This function has continuous rotational symmetry and, therefore, a continuous angular momentum. The momentum operator acts on the CEA state in M_2 which has a quasi-angular momentum due to its discrete rotational symmetry. This difference gives M_1 and M_2 distinct mathematical forms.

To proceed we focus on M_1 . We compute the momentum operator acting on the vector potential with a Laguerre-Gaussian radial profile as described in Eq. (10).

$$\mathbf{p} \cdot \mathbf{A}_{\sigma\ell}^{(+)} = i\hbar \left(\frac{\ell(\sigma-1)}{\sqrt{2}r} e^{-i\theta} + \frac{\sqrt{2}r}{w_0^2} e^{i\sigma\theta} \right) A_\ell(\mathbf{r}_\perp) e^{-i\omega t}. \quad (13)$$

This expression has been derived assuming that $\ell \geq 0$. The first term can then be thought as being only nonzero when the sign of the OAM is opposite to the sign of the SAM. This is known as *anti-parallel* twisted light.

We move into the rotating wave frame and assume the frequency of the light is equal to the frequency of the transition that is being driven (zero detuning). This eliminates the time dependence of Eq. (13). Then the first part of the matrix element takes the following form

$$\begin{aligned} M_1 &= -\frac{e i \hbar}{2m} \int d^3r \phi_{q\nu}^*(\mathbf{r}) Z_\nu^*(z) u_\nu(\mathbf{r})^* \times \\ &\left(\frac{\ell(\sigma-1)}{\sqrt{2}r} e^{-i\theta} + \frac{\sqrt{2}r}{w_0^2} e^{i\sigma\theta} \right) A_\ell(\mathbf{r}) \phi_{p\mu}(\mathbf{r}) Z_\mu(z) u_\mu(\mathbf{r}). \end{aligned} \quad (14)$$

The envelope function is slowly varying over the CEA whereas the unit cell function oscillates rapidly with the periodicity of the unit cell. The difference in the length scales of the functions allows the integral to be split into a product of two integrals: one over the entire CEA and one over each cell³³.

With this separation, the envelope functions can be integrated in the z axis. We find that

$$\int dz Z_\nu^*(z) Z_\mu(z) \approx 1. \quad (15)$$

This is the case due to the narrow confinement in the z direction which causes $Z(z)$ to be approximately the same normalised function irrespective of band.

With these assumptions, we find

$$\begin{aligned} M_1 &= -\frac{e i \hbar}{2m} \int_{a^3} d^3r u_\nu(\mathbf{r})^* u_\mu(\mathbf{r}) \times \\ &\int d^2r \phi_{q\nu}^*(\mathbf{r}) \left(\frac{\ell(\sigma-1)}{\sqrt{2}r} e^{-i\theta} + \frac{\sqrt{2}r}{w_0^2} e^{i\sigma\theta} \right) A_\ell(\mathbf{r}) \phi_{p\mu}(\mathbf{r}). \end{aligned} \quad (16)$$

The unit cell functions of each band are orthogonal to one another. This implies the first integral is zero unless the transition is between states within the same band.

$$\begin{aligned} M_1 &= -\frac{e i \hbar}{2m} \delta_{\nu,\mu} \times \\ &\int d^2r \phi_{q\nu}^*(\mathbf{r}) \left(\frac{\ell(\sigma-1)}{\sqrt{2}r} e^{-i\theta} + \frac{\sqrt{2}r}{w_0^2} e^{i\sigma\theta} \right) A_\ell(\mathbf{r}) \phi_{p\mu}(\mathbf{r}). \end{aligned} \quad (17)$$

We now turn our attention to the second part of the matrix element.

$$M_2 = -\frac{e}{2m} \times \int d^2r [\phi_{q\nu}^*(\mathbf{r}) Z_\nu^*(z)_\nu u_\nu(\mathbf{r})^*] A_\ell(\mathbf{r}) \hat{\epsilon}_\sigma \cdot i\hbar \nabla [\phi_{p\mu}(\mathbf{r}) Z_\mu(z)_\mu u_\mu(\mathbf{r})]. \quad (18)$$

As described above, we make the approximation that the integral is equal to the product of the two integrals on different length scales and integrate out the normalised Z function.

The inner product of the polarisation and the gradient creates two terms: one with the derivative of the transverse envelope function, the other with the derivative of unit cell function.

$$\begin{aligned} M_2 &= -\frac{i\hbar e}{2m} \left[\int_{a^3} d^3r u_\nu(\mathbf{r})^* u_\mu(\mathbf{r}) \int d^2r \phi_{q\nu}^*(\mathbf{r}) A_\ell(\mathbf{r}) [\hat{\epsilon}_\sigma \cdot \nabla \phi_{p\mu}(\mathbf{r})] + \right. \\ &\left. \int_{a^3} d^3r u_\nu(\mathbf{r})^* [\hat{\epsilon}_\sigma \cdot \nabla u_\mu(\mathbf{r})] \int d^2r \phi_{q\nu}^*(\mathbf{r}) A_\ell(\mathbf{r}) \phi_{p\mu}(\mathbf{r}) \right] \\ &= M_{2a} + M_{2b}. \end{aligned} \quad (19)$$

We first focus on M_{2a} . To this end, we compute the gradient in this term.

$$\begin{aligned} \hat{\epsilon}_\sigma \cdot \nabla \phi_{p\mu}(\mathbf{r}) &= \frac{A_{p\mu}}{\sqrt{2}\zeta_\mu^2} \sum_j [-(x-x_j) - i\sigma(y-y_j)] \chi_{j\mu}(\mathbf{r}_\perp) \varepsilon^{(j-1)p} \\ &= \frac{A_{p\mu}}{\sqrt{2}\zeta_\mu^2} \sum_j [\rho_0 e^{i\sigma\theta_j} - r e^{i\sigma\theta}] \chi_{j\mu}(\mathbf{r}_\perp) \varepsilon^{(j-1)p} \\ &= \frac{1}{\sqrt{2}\zeta_\mu^2} [\rho_0 \phi_{p+\sigma,\mu}(\mathbf{r}) - r e^{i\sigma\theta} \phi_{p\mu}(\mathbf{r})] \end{aligned} \quad (20)$$

where the Cartesian position of the j^{th} QD is (x_j, y_j) . From the second to the third line we have used the expression $e^{i\sigma\theta_j} = \varepsilon^{(j-1)\sigma}$.

We substitute Eq. (20) into the M_{2a} and use the orthonormality of the unit cell function to find

$$\begin{aligned} M_{2a} &= -\frac{e i \hbar}{2\sqrt{2}m\zeta_\mu^2} \delta_{\nu,\mu} \times \\ &\int d^2r \phi_{q\nu}^*(\mathbf{r}) A_\ell(\mathbf{r}) [\rho_0 \phi_{p+\sigma,\mu}(\mathbf{r}) - r e^{i\sigma\theta} \phi_{p\mu}(\mathbf{r})]. \end{aligned} \quad (21)$$

We now return to Eq. (19) and work on M_{2b} .

$$\begin{aligned} M_{2b} &= -\frac{e}{2m} \hat{\epsilon}_\sigma \cdot \int_{a^3} d^3r u_\nu(\mathbf{r})^* i\hbar \nabla u_\mu(\mathbf{r}) \times \\ &\int d^2r \phi_{q\nu}^*(\mathbf{r}) A_\ell(\mathbf{r}) \phi_{p\mu}(\mathbf{r}). \end{aligned} \quad (22)$$

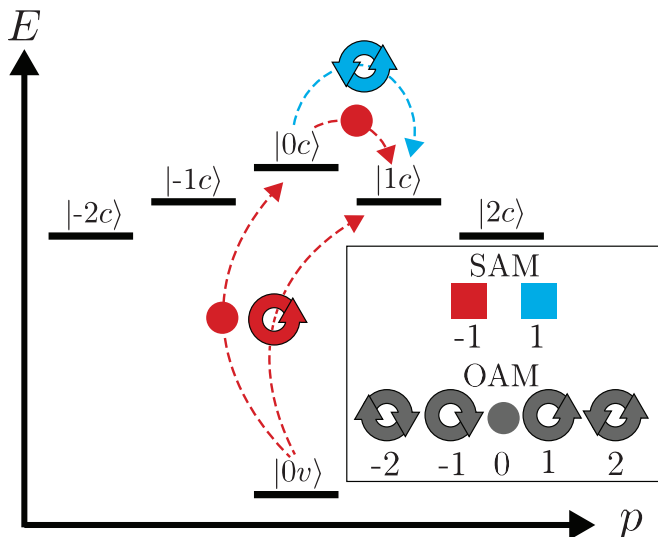


FIG. 2. The energy structure for a CEA composed of five QDs, including the angular momentum of the optical fields required to drive certain transitions. The SAM, encoded in the light's polarisation, is red (blue) for beams with -1 (+1) units of angular momentum; the OAM is depicted by orientation of the symbol presented for each transition. The two interband transitions are driven by circularly polarised light (SAM = +1) which accounts for the different electron spin between the two bands. Therefore only the optical field's OAM can drive transitions between states of different quasi-angular momentum. This is the case for transition from $|0v\rangle$ to $|1c\rangle$ which requires the driving light to have an OAM = 1. The transitions in the conduction band permit both the SAM and the OAM to alter the quasi-angular momentum. This means the transition within the conduction band from $|0c\rangle$ to $|1c\rangle$ can be driven by a *parallel* (SAM = +1, OAM = 0) or *anti-parallel* (SAM = -1, OAM = +2) optical field. In these last two transitions we note that as the initial state has a higher energy than the final state and, therefore, these transitions occurs by stimulated emission.

Let $\mathbf{p}_{\nu\mu} = \int_{a^3} d^3r u_\nu(\mathbf{r})^* i\hbar\nabla u_\mu(\mathbf{r})$. The magnitude of this momentum matrix element is specific to the semiconductor material of the QDs. It is only nonzero for interband transitions.

$$M_{2b} = -\frac{e}{2m} \hat{\epsilon}_\sigma \cdot \mathbf{p}_{\nu\mu} \int d^2r \phi_{q\nu}^*(\mathbf{r}) A_\ell(\mathbf{r}) \phi_{p\mu}(\mathbf{r}). \quad (23)$$

Some parts of the matrix element allows for transitions within the same band whilst other parts only allow transitions between bands. Figure 2 illustrates some of the possible transitions. In the next sections we explicitly organise our results into interband and intraband transitions.

Interband Transitions

We first concentrate on interband transitions. Of the total matrix element, Eq. (12), the only part that is

nonzero for transitions between bands is Eq. (23). This exact result for interband transition matrix elements has been calculated elsewhere³³, albeit with a different quantum system. We consider a transition from the conduction band ($\mu = c$) to the valence band ($\nu = v$) mediated by an optical emission with SAM σ and OAM ℓ . We denote the quasi-angular momentum of the initial and final state as p and q , respectively.

We have rescaled Eq. (23) to define a parameter that determines the relative magnitude of interband transitions

$$h_{pq;\ell}^{(\text{inter})} = \int d^2r A_\ell(\mathbf{r}) \phi_{q,c}^*(\mathbf{r}) \phi_{p,v}(\mathbf{r}). \quad (24)$$

It is noteworthy that only the OAM can drive transitions between states of different quasi-angular momentum. The SAM, encoded in the polarisation, accounts for the different spins of the valence and conduction band states³¹.

Intraband Transitions

We also examine transitions within a single band. The energy difference between two valence band states is approximately equal the interdot coupling energy t_v . This energy depends on the overlap between neighbouring QDs. The greater confinement in the valence band results in very limited overlap between the valence band wave functions of adjacent QDs. This will likely result in the valence band states being approximately degenerate for most CEAs. We therefore limit our study of intraband transitions to states within the conduction band. The intraband matrix element is the sum of Eq. (17) and Eq. (21). For a transition between an initial and final state with quasi-angular momentums p and q , respectively, we find

$$M_{pq;\sigma\ell}^{(\text{intra})} = -\frac{i\hbar e}{2m} \int d^2r A_\ell(\mathbf{r}) \phi_{p,c}^*(\mathbf{r}) \quad (25)$$

$$\left[\left(\frac{\sqrt{2}}{w_0^2} - \frac{\sqrt{2}\ell}{r^2} \delta_{\sigma,-1} - \frac{1}{\sqrt{2}\zeta_c^2} \right) r e^{i\sigma\theta} \phi_{p,c}(\mathbf{r}) + \frac{\rho_0}{\sqrt{2}\zeta_\mu^2} \phi_{p+\sigma,c}(\mathbf{r}) \right].$$

We once again rescale the matrix element to define a dimensionless parameter: $h_{pq;\sigma\ell}^{(\text{intra})} = -\zeta_c \frac{2m}{i\hbar e} M_{pq;\sigma\ell}^{(\text{intra})}$. This parameter will be used to determine the magnitude of transitions within the conduction band.

IV. OPTICAL RESPONSE

The theory developed in Sec. III is employed to explore the optical properties of CEAs. Parameters of importance include the radius of the CEA ρ_0 and the full width half maximums of the QDs, f_v and f_c . Current etching techniques permit precise control of the the position of QDs in a nanoscale array³⁹ and, therefore, precise

control of ρ_0 . The great variety of semiconductor materials coupled with the diversity of QD geometries permit some control of the the full width half maximums associated with the QD's wave functions^{40,41}.

An electron in the valence band experiences greater confinement than an electron in the conduction band. We therefore make the assumption that the full width half maximum of the QD wave function is greater in the conduction band than the valence band, $f_v < f_c$. We make the assumption that the beam waist w_0 of the light involved in the transition is equal to the radius of the CEA ρ_0 .

Throughout this section we represent the interband results in terms of its normalised transition magnitude $\tilde{f}|h^{\text{inter}}|$ where $\tilde{f} = \sqrt{f_v^2 + f_c^2}$. Similarly, the intraband result are expressed by the figure of merit $f_c|h^{\text{intra}}|$.

To form a CEA requires QDs in relatively close proximity such that the CEA's wave function takes the form of a delocalised, collective wave function and not an array of isolated QDs. Achieving significant overlap between neighbouring QDs requires maximising the length of its evanescent decay relative to the width of the physical QD. This can be realised with small QDs of diameter tens of nanometres; numerous semiconductor QDs have been fabricated within this size range⁴²⁻⁴⁵. However, the short distances that the QD's wavefunctions decay outside of the actual QD effectively limits the range ρ_0 . As this radius grows the QDs are further separated and the overlap between them is reduced. Therefore, CEAs composed of few QDs require a small radius. CEAs with larger radii can be achieved but they require more QDs. This paper does not investigate CEAs with greater than nine QDs. Thus, we assume ρ_0 is of order tens of nanometers.

Transitions were found to have a negligible magnitude unless the change in the CEAs quasi-momentum matched the angular momentum of the emitted light. This means for an interband transition from a state with quasi-angular momentum p to one with quasi-angular momentum q mediated by a optical source with OAM ℓ , we obtain the interband selection rule: $q - p = \ell$. Recall the SAM of the optical emission in interband transitions cannot affect the quasi-angular momentum of the electron's envelope function. However, for transitions within a single band the SAM can influence the quasi-angular momentum associated with the electron's envelope function. Thus intraband transitions mediated by light with SAM σ have the selection rule: $q - p = \sigma + \ell$.

We note that the energy difference between states will determine the frequency of the light that can be used to drive transitions. The interband energy difference is far greater than the intraband energy difference, thereby requiring a smaller wavelength of light to optically drive such transition.

Finally it is noteworthy that the prefactors for interband Eq. (23) and intraband Eq. (25) transitions are of similar magnitudes. This can be demonstrated with a brief calculation if, for example, one assumes $|\mathbf{p}_{vc} \cdot \hat{\epsilon}_\sigma| = 6.4 \times 10^{-25} \text{kg m/s}$ for GaAs³³.

Interband Transitions

The likelihood of any interband transition depends on the magnitude of h^{inter} in Eq. (24). Throughout this section we compute the magnitude of h^{inter} over the dimensionless parameter ρ_0/\tilde{f} . Simulations are only conducted for $\rho_0/\tilde{f} \geq 0.5$ as below this ratio the CEA loses its distinctive ring geometry.

We specifically consider transitions from excited electrons in the conduction band returning to the valence band. In our simulations the electron's conduction band quasi-angular momentum is equal to the OAM of the light emitted, as the selection rule demands. The final valence band state has no angular momentum in its envelope function.

The first parameters we explore are the full width half maximums of the QDs, see figure Eq. 3. Simulations in this figure hold $f_v = 10$ whilst varying f_c . The maximum h^{inter} attained for all simulations occurred at the ratio $\rho_0/\tilde{f} \approx 1$. At this ratio the wave function of the electron has a broad doughnut profile. This ratio of ρ_0/\tilde{f} determines a relationship between the CEA geometry and the QD wave function which can be tuned to maximise transition rates.

The simulations also revealed that the transition probability increased as f_c was decreased and, therefore, drew nearer to the f_v value. Furthermore, it was found that any simulation with the same ratio of f_c/f_v produced the same curve. We conclude that the magnitude of any interband transition will be maximised by minimising the difference between the two full width half maximums of the QDs. This is equivalent to minimising the difference between the electron and hole masses.

We also examine how the total amount of angular momentum exchanged influences the magnitude of a transition. Figure 4 presents these results. It demonstrates that the greater angular momentum exchanged, the greater ρ_0/\tilde{f} ratio at which the maximum transition strength occurs. This is explained by the profile of emitted light. Endowing light with greater quantities of OAM changes the radial profile of the light to have a greater intensity at its beam waist. The wave function matches the light's more concentrated radial profile better at a greater ρ_0/\tilde{f} ratio.

Thus maximising a transition of a particular quantity of angular momentum will require carefully selecting the CEA's radius ρ_0 .

The other notable feature of figure 4 is that transitions which exchange less angular momentum have a greater maximum transition strength. These transitions are therefore more probable. Thus CEAs may be limited in how great a quantity of OAM may be released in a single optical emission as multiple pulses of less angular momentum will be preferentially emitted.

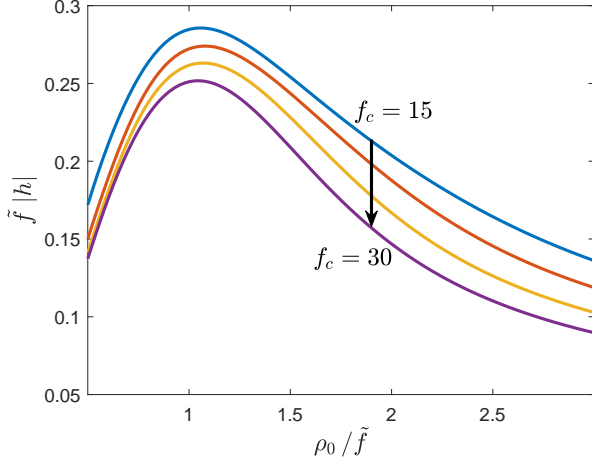


FIG. 3. The strength of the interband transition $|0v\rangle \rightarrow |2c\rangle$ (quantified by $\tilde{f}|h^{\text{inter}}|$ where h^{inter} is defined in Eq. 24) for varying QD widths. The strength of each transition is plotted against the normalised radius of the CEA, ρ_0/\tilde{f} . In each of the four data sets presented the QDs' valence band full width half maximum is held constant ($f_v = 10$) whereas its conduction band width is altered from $f_c = 15$ to $f_c = 30$. In the transition considered the optical field has OAM = 2 and the CEA consists of nine QDs. The greatest transition strength occurs at $\rho_0/\tilde{f} \approx 1$. Though transitions with smaller f_c have a greater maximum transition strength. Any transition with the same ratio f_c/f_v produced the same curve.

Intraband Transitions

The probability of any transition within a single band is determined by the parameter h^{intra} which is proportional to M^{intra} in Eq. (25). Both the light's SAM σ and OAM ℓ can change the quasi-angular momentum of the envelope function for intraband transition. Therefore, we must now consider the impact of parallel (sign $\sigma = \text{sign } \ell$) and anti-parallel (sign $\sigma = -\text{sign } \ell$) optical emissions.

Figure 5 displays two transitions mediated by both parallel and anti-parallel optical emissions. These transitions are $|2\rangle \rightarrow |1\rangle$ and $|2\rangle \rightarrow |0\rangle$. Our simulations revealed that the results are independent of f_c .

The simulations demonstrated that there exists a radius where each transition becomes the dominant one. This implies that precisely tuning the ρ_0/f_c ratio allows the engineering both the quantity and distribution of angular momentum in the optical emissions.

The transition from $|2\rangle \rightarrow |0\rangle$ (broken curves) generally reflects the transition from $|2\rangle \rightarrow |1\rangle$ (solid curve) albeit shifted to a greater ρ_0/f_c ratio. The greater angular momentum exchanged, in the former transition, requires the emitted light to carry away more OAM. Similarly to interband transitions, a greater OAM in the optical emission requires a more distinct ring profile of the wave function which occurs at greater ρ_0/f_c ratios.

It is likely that the CEA will be driven by circularly polarised light between states within the conduction band.

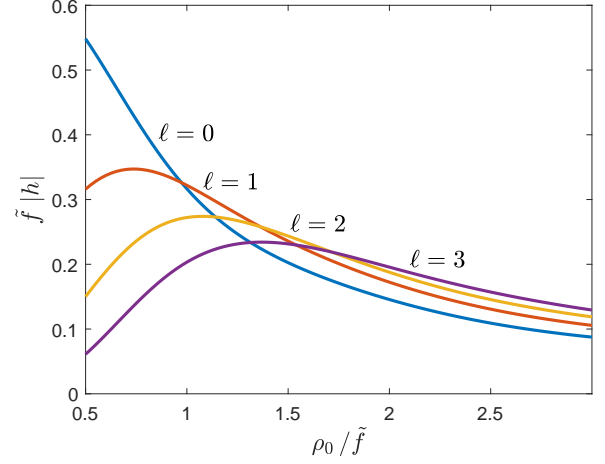


FIG. 4. The strength of interband transitions (quantified by $\tilde{f}|h^{\text{inter}}|$ where h^{inter} is defined in Eq. 24) with different quantities of angular momentum exchanged. The strength of each transition is plotted against the normalised radius of the CEA, ρ_0/\tilde{f} . The transitions shown are $|0v\rangle \rightarrow |lc\rangle$ mediated by an optical pulse with OAM $\ell \in [0, 3]$. The interband transition selection rule demands that the change in quasi-angular momentum must be equal to optical field's OAM. Transitions involving greater changes in the CEA's quasi-angular momentum have their maximum transition strength occur at a greater radius. This data was obtained for a CEA with nine emitters and full width half maximum ratio $f_v/f_c = 1/2$.

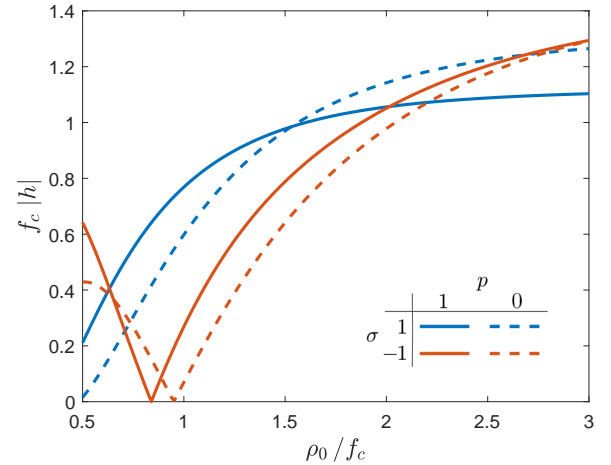


FIG. 5. The strength of intraband transitions (quantified by $f_c|h^{\text{intra}}|$ where h^{intra} is proportional to Eq. 25) mediated by optical fields with various angular momentum distributions. The strength of each transition is plotted against the normalised radius of the CEA, ρ_0/f_c . Two transitions are considered, each of the form $|2\rangle \rightarrow |p\rangle$; $p = 1$ is the solid line and $p = 0$ is the dashed line. In each transition we have the selection rule $\sigma + \ell = 2 - p$. The transition involving a parallel optical emission has $\sigma = 1$ and is plotted in blue. The anti-parallel transition ($\sigma = -1$) is plotted in red. In both transitions $\ell \geq 0$. The CEA in these simulations was composed of nine emitters.

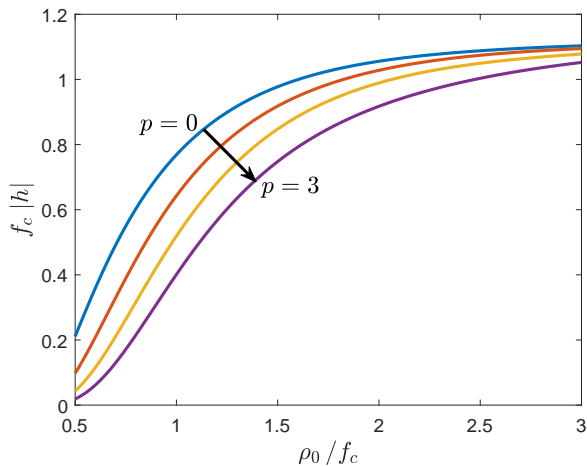


FIG. 6. The strength of intraband transitions (quantified by $f_c |h^{\text{intra}}|$ where h^{intra} is proportional to Eq. 25) is driven by circularly polarised light. The strength of each transition is plotted against the normalised radius of the CEA, ρ_0/f_c . A series of transitions mediated by circularly polarised light are considered each incrementing the quasi-angular momentum of the CEA by one unit. The transition are $|p\rangle \rightarrow |p+1\rangle$ where $p \in [0, 1, 2, 3]$, as indicated in the figure. Transitions involving states of greater quasi-angular momentum are slightly weaker. The CEA in these simulation was composed of nine emitters with $f_c = 20$.

Figure 6 displays the magnitude of transitions driven by circularly polarized light without OAM that increment the quasi-angular momentum of the CEA. That is, it drives the transition $|p\rangle \rightarrow |p+1\rangle$.

Each transition has a similar profile except the lower the initial quasi-angular momentum of the CEA state, the greater the transition magnitude. This suggests that driving a CEA to states of higher quasi-angular momentum becomes less probable with each transition.

V. DISCUSSION

The results presented in Section IV demonstrate a range of parameters that impact the optical properties of the CEA. We now use these results to outline design principles for CEAs. In particular, we consider a surface covered in CEAs to form a metamaterial. This metamaterial has been theorised to be able to upconvert optical angular momentum²⁶ and act as a twisted light laser²⁰.

For a CEA to absorb twisted light, the doughnut profile of the light must be aligned and of the same scale as the wave function of the CEA. Standard techniques for producing twisted light create light with a beam waist of hundreds of nanometres whereas we expect the radius of the CEA to be an order of magnitude smaller. Therefore, increasing the quasi-angular momentum of the CEA will involve driving it with circularly polarised light without OAM.

This process of the ‘banking’ of angular momentum by driving a CEA with circularly polarised light is the first step in the upconversion of optical angular momentum. The first circularly polarised light pulse is required to excite an electron from the valence band to the conduction band. Lets assume this transition is $|0v\rangle \rightarrow |0c\rangle$. This transition is displayed in figure 4 (the $\ell = 0$ curve). It is evidently possible as it happens with a non-zero magnitude. Literature on the common semiconductor material GaAs suggests that the energy difference between the two bands in QDs is approximately 1eV ³⁸. This suggests this first excitation pulse would need to be in the infrared spectrum.

The next stage in the process would be driving the CEA into the desired state in the conduction band. Circularly polarised light can only increment the quasi-angular momentum of the CEA one unit per transition. Hence, reaching CEA states of higher quasi-angular momentum requires more transitions. Figure 6 demonstrates that this process is possible as each of these transitions is of a similar magnitude. However, transitions to higher angular momentums have a lower magnitude. This suggest there is some limit to this process. Further limiting this process will be relaxation processes within the CEA.

According to Eq. (4) these transitions will require the energy of the photons to be $\hbar\omega \approx t_c$. The magnitude of this term has been estimated to be approximately 1meV for GaAs⁴⁶. This translates into photons between microwave and infrared frequencies.

We now consider the final step in the process of optical angular momentum upconversion. This is the emission of light with the desired angular momentum properties. There are a number of relaxation paths that a conduction band electron can take. Possible intraband transitions are depicted for the state $|2c\rangle$ in figure 5. This figure shows a region between $1.3 < \rho_0/f_c < 2.6$ where the transition $|2c\rangle \rightarrow |0c\rangle$ mediated by a parallel optical emission is stronger than other transitions. By ensuring the CEA’s radius met this criteria one could preferentially select this type of optical emission.

Figure 5 also demonstrates other transitions are of approximately equal strength. Further complicating the picture is that the specific QD selected will alter the results. However for a given QD with a known wave function, the theory developed in Section III can be applied to get precise results. Regardless, our results suggest that it is likely the metamaterial will emit light with different quantities of angular momentum and with a varying distribution between the SAM and OAM.

It is pertinent that the magnitudes of intraband transitions (figure 5) are greater than the strength of the interband transitions (figure 3). This suggests that the metamaterial will emit twisted light but the electron will remain within the conduction band. By driving the CEAs with a circularly polarised broadband beam, with centre frequency t_c/\hbar , one could achieve continuous emission of twisted light. The driving light source could continually

promote the electron to higher quasi-angular momentum states each time it emitted twisted light. Combining the metamaterial with a filter to select the particular type of twisted light desired could be the basis for a device that upconverts circularly polarised light into twisted light. The efficiency of such a device would depend on the relative magnitude of the desired transition compared to all other relaxation pathways.

VI. CONCLUSION

In this paper we have analytically found the expressions for interband and intraband transitions within CEAs. The strength of transitions mediated by optical fields with various amounts and distributions of angular momentum has been determined. Simulations revealed the effect of the CEAs geometry on the magnitude of different transitions.

Furthermore, selection rules were derived. For transitions between bands it was shown that the change in the CEA's quasi-angular momentum must equal the optical field's OAM. Whereas for intraband transitions, the change in quasi-angular momentum must equal the sum of the SAM and OAM.

A metamaterial for the upconversion of optical angular momentum has been discussed. We suggest such a device could be fabricated which, when driven by circularly polarised light of the right frequency, could emit twisted light. Combined with appropriate optical filter, such a device could be made that produced the desired twisted light in a continuous or pulsed mode.

VII. ACKNOWLEDGMENTS

We would like to thank Ben Baragiola and Andy Greentree for the useful discussion. The authors acknowledge the support of the Australian Research Council through grant CE170100026. This research was undertaken with the assistance of resources and services from the National Computational Infrastructure, which is supported by the Australian Government.

Appendix: Normalisation

To compute the normalisation of the transverse envelope function we require the parameter $t_{m\nu}$. This is the overlap between the basis functions of two QDs that are m QDs away from each other in the CEA. We note that $t_{1\nu} = t_\nu$.

$$t_{m\nu} = \int d^2r \chi_{m,\nu} \chi_{m+n,\nu} = e^{-(d_m/2s_\nu)^2}, \quad (\text{A.1})$$

where d_m is the distance between QDs

$$d_m = \rho_0 \sqrt{2 \left[1 - \cos \left(\frac{2\pi m}{N} \right) \right]}. \quad (\text{A.2})$$

The normalisation constant $\mathcal{A}_{q\nu}$ for the envelope function is:

$$\int d^2r |\psi_{q\nu}|^2 = |\mathcal{A}_{q\nu}|^2 \int d^2r \sum_{j,k} \chi_{j\nu} \chi_{k\nu} \varepsilon^{(j-k)q} \quad (\text{A.3})$$

With some work it can then be shown that

$$\mathcal{A}_{q\nu} = N^{-1/2} \times \left[1 + 2 \sum_m t_{m\nu} \cos \left(\frac{2\pi m q}{N} \right) + t_{\frac{N}{2}\nu} \cos(\pi q) \delta_{N(\text{mod } 2),0} \right]^{-1/2}. \quad (\text{A.4})$$

We see from the δ function that the last term in Eq. (A.4) is non-zero only for CEAs with an even number of QDs.

* hugh.sullivan@rmit.edu.au

† jared.cole@rmit.edu.au

¹ J. H. Poynting, The wave motion of a revolving shaft, and a suggestion as to the angular momentum in a beam of circularly polarised light 82 proceedings of the royal society of london. series a, containing papers of a mathematical and physical character <http://doi.org/10.1098/rspa.1909.0060>, Proceedings of the Royal Society of London. Series A **82** (1909).

² R. A. Beth, Mechanical detection and measurement of the angular momentum of light, Physical Review **50**, 115 (1936).

³ L. Allen, M. W. Beijersbergen, R. Spreeuw, and J. Woerdman, Orbital angular momentum of light and the transformation of laguerre-gaussian laser modes, Physical Review

A **45**, 8185 (1992).

⁴ D. L. Andrews and M. Babiker, *The angular momentum of light* (Cambridge University Press, 2012).

⁵ J. P. Torres and L. Torner, *Twisted photons: applications of light with orbital angular momentum* (John Wiley & Sons, 2011).

⁶ H. Rubinsztein-Dunlop, A. Forbes, M. V. Berry, M. R. Dennis, D. L. Andrews, M. Mansuripur, C. Denz, C. Alpmann, P. Banzer, T. Bauer, *et al.*, Roadmap on structured light, Journal of Optics **19**, 013001 (2016).

⁷ G. Knöner, S. Parkin, T. A. Nieminen, V. L. Loke, N. R. Heckenberg, and H. Rubinsztein-Dunlop, Integrated optomechanical microelements, Optics express **15**, 5521 (2007).

⁸ J. Geng, Structured-light 3d surface imaging: a tutorial,

- Advances in Optics and Photonics **3**, 128 (2011).
- ⁹ N. Radwell, G. Walker, and S. Franke-Arnold, Cold-atom densities of more than 10^{12} cm^{-3} in a holographically shaped dark spontaneous-force optical trap, *Physical Review A* **88**, 043409 (2013).
 - ¹⁰ C. Rosales-Guzmán, N. Hermosa, A. Belmonte, and J. P. Torres, Experimental detection of transverse particle movement with structured light, *Scientific reports* **3**, 1 (2013).
 - ¹¹ Y. Yan, G. Xie, M. P. Lavery, H. Huang, N. Ahmed, C. Bao, Y. Ren, Y. Cao, L. Li, Z. Zhao, *et al.*, High-capacity millimetre-wave communications with orbital angular momentum multiplexing, *Nature communications* **5**, 4876 (2014).
 - ¹² M. Erhard, R. Fickler, M. Krenn, and A. Zeilinger, Twisted photons: new quantum perspectives in high dimensions, *Light: Science & Applications* **7**, 17146 (2018).
 - ¹³ M. Padgett, J. Courtial, and L. Allen, Light's orbital angular momentum, *Physics Today* **57**, 35 (2004).
 - ¹⁴ A. Niv, G. Biener, V. Kleiner, and E. Hasman, Spiral phase elements obtained by use of discrete space-variant subwavelength gratings, *Optics communications* **251**, 306 (2005).
 - ¹⁵ N. Yu, P. Genevet, M. A. Kats, F. Aieta, J.-P. Tetienne, F. Capasso, and Z. Gaburro, Light propagation with phase discontinuities: generalized laws of reflection and refraction, *science* **334**, 333 (2011).
 - ¹⁶ K. E. Chong, I. Staude, A. James, J. Dominguez, S. Liu, S. Campione, G. S. Subramania, T. S. Luk, M. Decker, D. N. Neshev, *et al.*, Polarization-independent silicon metadevices for efficient optical wavefront control, *Nano letters* **15**, 5369 (2015).
 - ¹⁷ A. Žukauskas, M. Malinauskas, and E. Brasselet, Monolithic generators of pseudo-nondiffracting optical vortex beams at the microscale, *Applied Physics Letters* **103**, 181122 (2013).
 - ¹⁸ X. Cai, J. Wang, M. J. Strain, B. Johnson-Morris, J. Zhu, M. Sorel, J. L. O'Brien, M. G. Thompson, and S. Yu, Integrated compact optical vortex beam emitters, *Science* **338**, 363 (2012).
 - ¹⁹ P. Miao, Z. Zhang, J. Sun, W. Walasik, S. Longhi, N. M. Litchinitser, and L. Feng, Orbital angular momentum microlaser, *Science* **353**, 464 (2016).
 - ²⁰ M. D. Williams, M. M. Coles, D. S. Bradshaw, and D. L. Andrews, Direct generation of optical vortices, *Physical Review A* **89**, 033837 (2014).
 - ²¹ M. M. Coles, M. D. Williams, K. Saadi, D. S. Bradshaw, and D. L. Andrews, Chiral nanoemitter array: A launchpad for optical vortices, *Laser & Photonics Reviews* **7**, 1088 (2013).
 - ²² M. D. Williams, M. M. Coles, K. Saadi, D. S. Bradshaw, and D. L. Andrews, Optical vortex generation from molecular chromophore arrays, *Physical review letters* **111**, 153603 (2013).
 - ²³ R. Songmuang, S. Kiravittaya, and O. G. Schmidt, Formation of lateral quantum dot molecules around self-assembled nanoholes, *Applied physics letters* **82**, 2892 (2003).
 - ²⁴ S. J. Barrow, A. M. Funston, X. Wei, and P. Mulvaney, Dna-directed self-assembly and optical properties of discrete 1d, 2d and 3d plasmonic structures, *Nano Today* **8**, 138 (2013).
 - ²⁵ J. V. Barth, G. Costantini, and K. Kern, Engineering atomic and molecular nanostructures at surfaces, in *Nanoscience and technology: a collection of reviews from Nature journals* (World Scientific, 2010) pp. 67–75.
 - ²⁶ X. Zang and M. T. Lusk, Twisted molecular excitons as mediators for changing the angular momentum of light, *Physical Review A* **96**, 013819 (2017).
 - ²⁷ X. Zang and M. T. Lusk, Angular momentum transport with twisted exciton wave packets, *Physical Review B* **96**, 155104 (2017).
 - ²⁸ J. M. Pietryga, Y.-S. Park, J. Lim, A. F. Fidler, W. K. Bae, S. Brovelli, and V. I. Klimov, Spectroscopic and device aspects of nanocrystal quantum dots, *Chemical reviews* **116**, 10513 (2016).
 - ²⁹ X. Ma, M. Pu, X. Li, C. Huang, W. Pan, B. Zhao, J. Cui, and X. Luo, Optical phased array radiating optical vortex with manipulated topological charges, *Optics express* **23**, 4873 (2015).
 - ³⁰ P. Kotetes, P.-Q. Jin, M. Marthaler, and G. Schön, Circular-polarization-sensitive metamaterial based on triple-quantum-dot molecules, *Physical review letters* **113**, 236801 (2014).
 - ³¹ G. F. Quinteiro and P. I. Tamborenea, Theory of the optical absorption of light carrying orbital angular momentum by semiconductors, *EPL (Europhysics Letters)* **85**, 47001 (2009).
 - ³² G. F. Quinteiro and P. I. Tamborenea, Twisted-light-induced optical transitions in semiconductors: Free-carrier quantum kinetics, *Physical Review B* **82**, 125207 (2010).
 - ³³ G. F. Quinteiro and P. I. Tamborenea, Electronic transitions in disk-shaped quantum dots induced by twisted light, *Physical Review B* **79**, 155450 (2009).
 - ³⁴ G. F. Quinteiro and T. Kuhn, Light-hole transitions in quantum dots: Realizing full control by highly focused optical-vortex beams, *Physical Review B* **90**, 115401 (2014).
 - ³⁵ G. F. Quinteiro and J. Berakdar, Electric currents induced by twisted light in quantum rings, *Optics express* **17**, 20465 (2009).
 - ³⁶ B. Sbierski, G. F. Quinteiro, and P. I. Tamborenea, Twisted-light-induced intersubband transitions in quantum wells at normal incidence, *Journal of Physics: Condensed Matter* **25**, 385301 (2013).
 - ³⁷ T.-P. Hsieh, J.-I. Chyi, H.-S. Chang, W.-Y. Chen, T. M. Hsu, and W.-H. Chang, Single photon emission from an InGaAs quantum dot precisely positioned on a nanoplane, *Applied physics letters* **90**, 073105 (2007).
 - ³⁸ P. Harrison *et al.*, *Quantum wells, wires and dots* (Wiley Online Library, 2016).
 - ³⁹ V. Verma and J. Coleman, High density patterned quantum dot arrays fabricated by electron beam lithography and wet chemical etching, *Applied Physics Letters* **93**, 111117 (2008).
 - ⁴⁰ S. M. Reimann and M. Manninen, Electronic structure of quantum dots, *Reviews of modern physics* **74**, 1283 (2002).
 - ⁴¹ L. Jacak, P. Hawrylak, and A. Wojs, *Quantum dots* (Springer Science & Business Media, 2013).
 - ⁴² K. Deppert and L. Samuelson, Self-limiting transformation of monodisperse Ga droplets into GaAs nanocrystals, *Applied physics letters* **68**, 1409 (1996).
 - ⁴³ K. Alchalabi, D. Zimin, G. Kostorz, and H. Zogg, Self-assembled semiconductor quantum dots with nearly uniform sizes, *Physical review letters* **90**, 026104 (2003).
 - ⁴⁴ A. Yanes, J. Del Castillo, M. Torres, J. Peraza, V. Rodriguez, and J. Méndez-Ramos, Nanocrystal-size selective spectroscopy in $\text{SnO}_2:\text{Eu}^{3+}$ semiconductor quantum dots,

- Applied physics letters **85**, 2343 (2004).
- ⁴⁵ W. Ma, S. L. Swisher, T. Ewers, J. Engel, V. E. Ferry, H. A. Atwater, and A. P. Alivisatos, Photovoltaic performance of ultrasmall pbse quantum dots, ACS nano **5**, 8140 (2011).
- ⁴⁶ S. Yang, X. Wang, and S. D. Sarma, Generic hubbard model description of semiconductor quantum-dot spin qubits, Physical Review B **83**, 161301 (2011).